

The Color and Brightness of the F-corona Inferred from the 2019 July 2 Total Solar Eclipse

Benjamin Boe ¹ , Shadia Habbal ¹ , Cooper Downs ² , and Miloslav Druckmüller ³ Institute for Astronomy, University of Hawaii, Honolulu, HI 96822, USA; bboe@hawaii.edu ² Predictive Science Inc., San Diego, CA 92121, USA ³ Faculty of Mechanical Engineering, Brno University of Technology, Technicka 2, 616 69 Brno, Czech Republic Received 2021 January 27; revised 2021 February 23; accepted 2021 February 25; published 2021 May 3

Abstract

Total solar eclipses (TSEs) provide a unique opportunity to quantify the properties of the K-corona (electrons), F-corona (dust), and E-corona (ions) continuously from the solar surface out to a few solar radii. We apply a novel inversion method to separate emission from the K- and F-corona continua using unpolarized total brightness (tB) observations from five 0.5 nm bandpasses acquired during the 2019 July 2 TSE between 529.5 and 788.4 nm. The wavelength dependence relative to the photosphere (i.e., color) of the F-corona itself is used to infer the tB of the K- and F-corona for each line of sight. We compare our K-corona emission results with the Mauna Loa Solar Observatory (MLSO) K-Cor polarized brightness (pB) observations from the day of the eclipse, and the forward modeled K-corona intensity from the Predictive Science Inc. (PSI) magnetohydrodynamic (MHD) model prediction. Our results are generally consistent with previous work and match both the MLSO data and PSI-MHD predictions quite well, supporting the validity of our approach and of the PSI-MHD model. However, we find that the tB of the F-corona is higher than expected in the low corona, perhaps indicating that the F-corona is slightly polarized—challenging the common assumption that the F-corona is entirely unpolarized.

Unified Astronomy Thesaurus concepts: Solar corona (1483); Solar eclipses (1489); Solar F-corona (1991); Solar K-corona (2042); Solar optical telescopes (1514)

1. Introduction

Coronal emission in the visible wavelength range consists of broadband "continuum" emission, overlaid with a number of discrete spectral lines. Line emission is useful for studying various physical processes in the corona (e.g., Habbal et al. 2011, 2013; Ding & Habbal 2017; Boe et al. 2018, 2020a; Del Zanna et al. 2019), as it arises from the collisional and radiative excitation of various atomic and ionic species. Line emission is rather faint compared with the total coronal brightness, however, and occurs only at well-defined wavelengths, making it straightforward to separate it from the continuum brightness.

Continuum emission in the corona at visible wavelengths originates from two sources, each of which are physically interesting for different reasons. First, there is Thompson scattering of photospheric light by free electrons throughout the corona (e.g., van de Hulst 1950), known as the K-corona. Second, there is dust throughout the solar system that scatters and/or diffracts photospheric light (e.g., Koutchmy & Lamy 1985), called the F-corona. Both the K- and F-corona originate via the redirection of photospheric light, and so have a spectrum roughly proportional to the solar photosphere. The wavelength overlap and similar behavior of the K- and F-corona make them somewhat more challenging to isolate from each other, a task that is essential to investigate their physical characteristics.

The most common method for differentiating K- and F-corona emission has been to compare polarized brightness (pB) and total brightness (tB) observations (e.g., Ney et al. 1961; Morgan & Habbal 2007), because the K-corona is substantially polarized as a result of the scattering geometries (Minnaert 1930; Baumbach 1938). The K-corona is not completely polarized, however, so isolating the F-corona brightness requires an inversion method to infer the tB of the K-corona with a pB observation and a model of the polarization fraction (see Lamy et al. 2020 for a detailed

discussion). Another, more historical method to isolate the K- and F-corona emission is by observing the relative depth of Fraunhofer lines in the corona. Fraunhofer lines are the photospheric absorption lines present in the solar spectrum, which are retained in the dust scattering (e.g., van de Hulst 1950). The K-corona does not have these lines, as the high kinetic temperature of electrons ($T_e \sim 10^6$ K) in the corona smooths out the scattered solar spectrum in the K-corona. In fact, the names K-and F-corona refer to exactly this effect (in German)—K is "Kontinuierliche" and refers to its smooth continuous spectrum, while F is "Fraunhofer" for the presence of these photospheric lines. However, some broad Fraunhofer lines, such as Ca II H and K, do leave small, temperature-dependent variations in the K-corona spectrum (Cram 1976) that have been used to infer the coronal electron temperature (Reginald et al. 2003, 2009).

The spatially dependent scattering of the K-corona—depending both on the plane-of-sky distance from the Sun, or elongation angle (often referred to as the "impact parameter"), and the location of structures along the line of sight (LOS)—enables the characterization of three-dimensional (3D) structures like streamers (e.g., Kramar et al. 2014) and coronal mass ejections (CMEs; e.g., Moran & Davila 2004; Dere et al. 2005; Howard & Tappin 2009), especially if the event is observed from multiple viewing angles around the Sun (e.g., Colaninno & Vourlidas 2009; Moran et al. 2010; DeForest et al. 2017). Such pB inversion methods have been extensively used to infer the electron density in the corona (e.g., Allen 1947; Guhathakurta et al. 1996; Skomorovsky et al. 2011; Morgan & Cook 2020). Techniques have been developed to infer the electron density from total brightness (tB) observations as well (Hayes et al. 2001), though such methods require an assumed F-corona contribution to the continuum. Fine-scale density structures observed in tB emission of the K-corona have also been used to trace the coronal magnetic field topology (Boe et al. 2020b).

Although observing K-corona emission is propitious for coronal research, F-corona emission is typically more relevant to solar system science as a constraint on interplanetary dust (e.g., Leinert & Grün 1990). Indeed, the F-corona is often referred to simply as the component of zodiacal light that has the smallest elongation angles from Sun center (e.g., Kimura & Mann 1998). Unlike the K-corona, which originates from the scattering of free electrons close to the Sun, the F-corona is originating from dust along the entire LOS, from the Sun to 1 au and beyond (e.g., van de Hulst 1947; Mann 1998). This large LOS depth of the F-corona (i.e., zodiacal light) likely explains why the F-corona has been found to remain almost constant throughout the solar cycle (Morgan & Habbal 2007). There remains some uncertainty as to the behavior of dust particles near the Sun, and it is expected that the dust should vaporize in the vicinity of the Sun within a distance range referred to as the "dust-free zone" (e.g., Lamy 1974; Mukai et al. 1974). The size and dynamics of this dust-free zone have not been observationally characterized, but there are early observations from Parker Solar Probe that perhaps support its existence (Howard et al. 2019).

Another important difference between K- and F-corona emission is color. Throughout this article, we will use color to refer to the spectral intensity of the K- and F-corona with respect to the photospheric spectrum at different wavelengths (for each LOS), rather than the absolute intensity. That is to say, we are interested in wavelength-dependent scattering efficiency as a way to probe the spatially distributed properties of the dust and electrons (see Section 2.1 for more discussion). The K-corona will have a roughly neutral color relative to the photospheric spectrum, as Thompson scattering itself has no wavelength dependence though there is a small K-corona color effect resulting from the color dependence of limb-darkening (see Quémerais & Lamy 2002; Howard & Tappin 2009, Section 3.1). Conversely, the F-corona is substantially reddened due to dust diffraction (van de Hulst 1947), and will have a somewhat different color depending on the mineralogy of the scattering particles (Roeser & Staude 1978).

In this work, we introduce a novel inversion technique to isolate the K- and F-corona brightness via a color analysis. We used five unique narrowband observations of the coronal continuum between 529.5 and 788.4 nm from the 2019 July 2 total solar eclipse (TSE) (see Section 2.1), combined with the corresponding Mauna Loa Solar Observatory (MLSO) COronal Solar Magnetism Observatory (COSMO) K-coronagraph (K-Cor) polarized coronagraph data (see Section 2.2). In Section 3 we describe this novel inversion technique, followed by a discussion of our inferred color of the F-corona (see Section 4.1) and brightness of the K- (see Section 4.2) and F-corona (4.3), and compare with the Predictive Science Inc. (PSI) magnetohydrodynamic (MHD) model of the eclipse corona (see Section 2.3), as well as earlier published work (see Section 4). Concluding remarks are given in Section 5.

2. Data

2.1. Eclipse Observations

The eclipse data used in this work were acquired during the 2019 July 2 TSE in Chile and Argentina. There were three observing sites stationed along the path of totality, to increase the likelihood of clear skies. Specifically, observations were made in Chile at Cerro Tololo and Mammalluca, as well as in

Rodeo in Argentina. All the eclipse data used in this work are shown in Figure 1, with observing metadata included in Table 1. The data as shown in this figure are transformed into a Cartesian representation of polar coordinates by binning the original data into wedges with radial steps of $0.02~R_{\odot}$ and a width of 3° in latitude. The photometric imaging data are averaged inside each of these bins to increase the signal-tonoise ratio (S/N). This procedure will cause more pixels to be co-added at larger heliocentric distances, which will help to compensate for the decreasing S/N with distance (due to the decreasing coronal brightness).

Each telescope is outfitted with a 0.5 nm bandpass Fabry-Pérot filter to record the coronal emission at a precise wavelength. To isolate emission from the ions alone, each ionic line that is observed has an additional imaging system with a bandpass shifted to the nearby continuum. In making these continuum observations, we have serendipitously recorded the relative continuum emission in the corona at well-defined wavelengths across the visible spectrum, which is the focus of this work. We will not consider the line emission observations here. A detailed description of the design and operation of these narrowband Fabry-Pérot telescopes is given in Boe et al. (2020a). The exact same procedure is applied to the data in this work. We use some of the same telescopes (i.e., Fe XI, Fe XIV, and Ar X, see Table 1) that were described in Boe et al. 2020a, as well as a few additional ones (i.e., Fe X and Ni XV). The image alignment and stacking procedure is described in Druckmüller (2009).

The sky brightness is removed by measuring and subtracting the intensity observed at the center of the Moon during the eclipse. There will be a slight brightness from the Moon due to earthshine, which will vary depending on the geography of the Moon-facing side of the Earth (e.g., oceans are darker than land or snow). From the calculations of Agrawal (2016), we take the earthshine to be $2.5 \times 10^{-10} \pm 1.5 \times 10^{-10} I_{\odot}$ for all wavelengths (it will be a continuum source like the corona itself). This intensity is rather small compared with the lower corona, so this estimate will have a noticeable impact only on the results at high elongations ($\sim 2.5-3~R_{\odot}$).

To photometrically calibrate the eclipse data, we use the MLSO COSMO K-Cor data (see Section 2.2 and Figure 1) after they have been corrected by the polarized brightness fraction (pB/tB)from the PSI-MHD model (see Section 2.3) and corrected for limb-darkening effects (see Section 3.1). The K-Cor data are calibrated to be in units of the solar disk center intensity already, so they can be used as a calibration source for the eclipse data though the eclipse observations are able to probe significantly farther into the corona (out to $>2.5 R_{\odot}$) than the MLSO coronagraph ($<1.5 R_{\odot}$). To do this cross-calibration, we take the intensity in a 10° wedge from 1.125 to 1.15 R_{\odot} in the eastern streamer, because it had the lowest F/K ratio, and normalize all the eclipse data to the K-Cor data in this wedge. Implicit in this assumption is that the F-corona intensity is negligible within this wedge, which may not be the case. In Section 3.2, we present a method for isolating the F-corona in the tB eclipse observations, then iterate the procedure to account for the F/K calibration offset in Section 3.3.

It is important to note that this calibration process is performed in units of the solar disk center intensity at the given wavelength, which normalizes any dependence of the solar disk spectrum on the brightness observations presented here. In this way, we are working with the relative scattering of the incoming solar

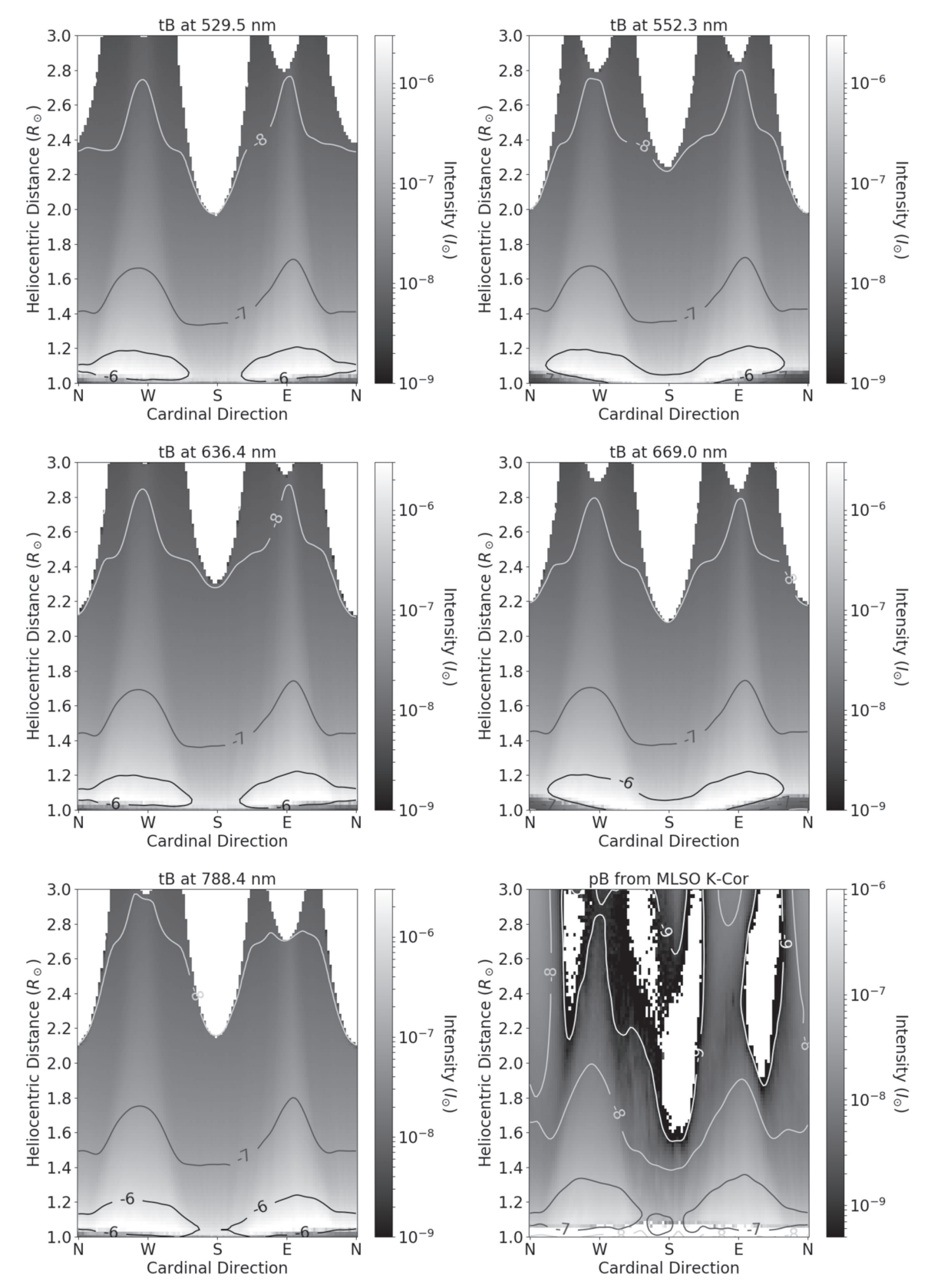


Figure 1. Total brightness (*tB*) of the continuum corona at each of the five narrowband wavelengths (see Section 2.1), arranged in increasing wavelength from left to right, top to bottom. The bottom right panel shows the observed polarized brightness (*pB*) of the corona from the MLSO COSMO K-Cor (see Section 2.2). Contours are shown for each integer of brightness in log space. The eclipse data are calibrated using the procedure described in Section 3, and are given in units of solar disk center intensity (for each wavelength). Metadata about the eclipse observations are included in Table 1.

Table 1
Observing Metadata for the 2019 July 2 Total Solar Eclipse Observations Used in This Work

λ (nm)	Aperture (cm)	Line	Observing Site	Length of Totality	Observers
529.5	7	Fe XIV	Rodeo, Argentina	2 ^m 14 ^s	Judd Johnson and Pavel Štarha
552.3	7	Ar X	Mammalluca, Chile	2 ^m 21 ^s	Martina Arndt, Rydia Hayes, Sarah Auriemma and Benedikt Justen
636.4	7	Fe X	Rodeo, Argentina	2 ^m 14 ^s	Judd Johnson and Pavel Štarha
669.0	5	Ni XV	Cerro Tololo, Chile	2 ^m 3 ^s	Petr Štarha and Jana Hodérova
788.4	7	Fe XI	Rodeo, Argentina	2 ^m 14 ^s	Judd Johnson and Pavel Štarha

radiation, which provides information about the physical properties of the scattering particles (i.e., dust and electrons) that we are interested in here. The absolute intensity of the corona will depend on the incoming solar photospheric spectrum as well, but the absolute intensity itself is not directly relevant to this work.

For wavelengths in the vicinity of rather large Fraunhofer lines, there will be a temperature-dependent effect where the K-corona spectrum can change somewhat due to a variable broadening of the lines. In fact, this effect has been previously used to infer the electron temperature in the low corona with spectroscopic eclipse observations (Reginald et al. 2003, 2009). However, this effect will be noticeable only for small elongation angles (<1.3 R_{\odot}) and in the vicinity of very deep Fraunhofer lines, such as Ca II H and K (396.9 and 393.3 nm respectively; Cram 1976), which is not the case for the bandpasses used in this work. Moreover, our calibration is relative to the disk center intensity integrated over the bandpass (via the MLSO K-Cor cross-calibration), so any effect from sufficiently small Fraunhofer lines on the integrated intensity is already accounted for.

This method of cross-calibration also accounts for the wavelength-dependent absorption by the Earth's atmosphere in the observations, as the observed intensity within the calibration wedge itself is convolved with the atmospheric attenuation. The atmospheric effects will be angle dependent across the sky, but we can assume a constant absorption fraction across the eclipse images, given that the field of view is within the small-angle approximation regime.

2.2. MLSO COSMO K-COR

In addition to the observed total brightness of the corona at the various wavelengths during the 2019 TSE (as described in Section 2.1), we used the ground-based coronagraph observations from the MLSO's COSMO K-Cor.⁴ The COSMO K-Cor instrument observes the polarized brightness (pB) of the corona on a daily basis in the lower regions of the corona starting above $\sim 1.1~R_{\odot}$ with a wavelength bandpass between about 720 and 750 nm. The design and characterization of the polarimeters for K-Cor are described in Hou et al. (2013). The K-Cor data are calibrated to solar disk center intensity units, and so they are a useful source for cross-calibrating the eclipse data (as done in Section 3).

To improve the quality of the K-Cor data, we averaged all available images for the entire day of 2019 July 2, as shown in Figure 1. Stacking the K-Cor data helped to reduce any sky brightness effects, and to increase the signal of the corona. Still,

the K-Cor data clearly have nonphysical features present above about $1.3~R_{\odot}$ in some regions of the data, probably due to imperfect subtraction of the Earth's atmospheric brightness (see Section 4.2). This approach will smooth any changes in the corona over this period. We can safely assume a static corona over this time period, however, as we do not expect any large changes over a few hours from the solar rotation, and no CMEs were observed on this day.

2.3. PSI-MHD Model

In addition to the observational data described earlier in this section, we also use a state-of-the-art high-resolution magnetohydrodynamic (MHD) model of the global corona on 2019 July 2, posted by the PSI group one week before totality.⁵ This simulation used a similar setup to the 2017 August 21 eclipse prediction, which is described in Mikić et al. 2018. This includes a wave-turbulence-driven (WTD) approach to specify coronal heating and a novel energization technique to add fieldaligned currents (shear/twist) over large-scale polarity inversion lines. Based on a quantitative comparison of the 2017 prediction to coronagraph observations (Lamy et al. 2019), small updates were made to the 2019 parameterization of the WTD model to increase the overall electron density of the model. This included a slight increase in the WTD Poynting flux at the inner boundary (increased heating), and a switch to using hybrid abundances in the radiative loss calculation (Landi et al. 2012; Schmelz et al. 2012).

To model the corona at a given time, a full-Sun map of the radial component of the photospheric magnetic field at the inner boundary must be specified. Because of the lead time required for publishing the prediction, this simulation used a splice of synoptic map data from the Solar Dynamics Observatory/Helioseismic and Magnetic Imager (Scherrer et al. 2012) based on what was available about 15 days prior to the eclipse. This map combined data for Carrington rotation 2217 with near-real-time data from a part of Carrington rotation 2218. To capture plume-like density structures at the poles, the polar caps were also filled with a random flux distribution whose net value matches observations of the net flux at high latitudes (also similar to Mikić et al. 2018). All told, the measurements span approximately 2019 May 22 to June 17, which places the oldest data near the west limb during totality.

Here we will use the forward modeled total and polarized LOS integrated brightness for the K-corona from the model. It is important to remark that the PSI-MHD model does not contain any dust, and so is a prediction of the K-corona intensity alone, without any contribution from the F-corona. The *tB* and *pB* of the K-corona (for 529.5 nm) according to the

⁴ K-Cor DOI:10.5065/D69G5JV8; https://mlso.hao.ucar.edu/mlso_data_calendar.php.

www.predsci.com/eclipse2019

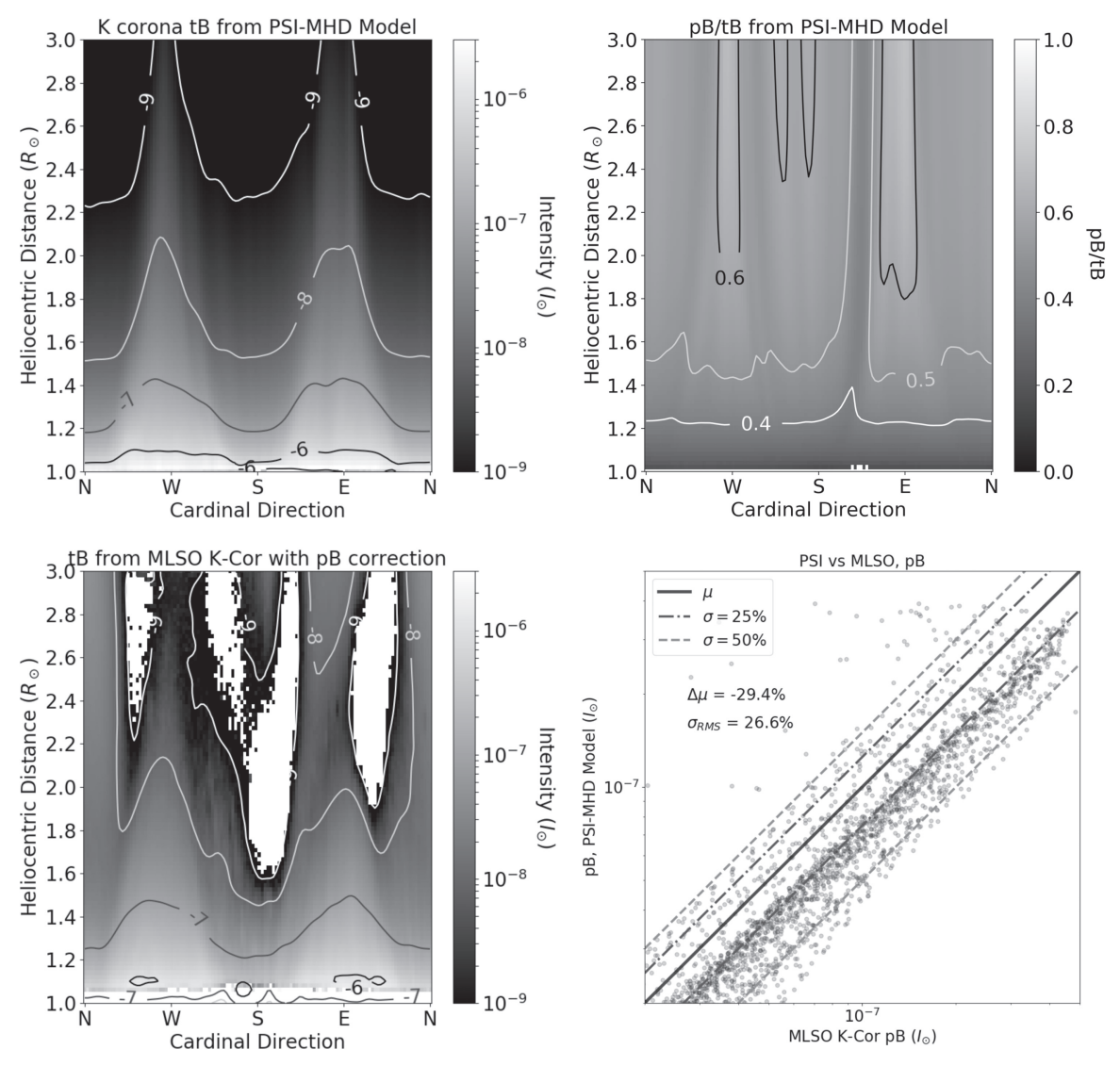


Figure 2. Top left: Predicted tB of the K-corona from the PSI-MHD model at 529.5 nm (see Section 2.3). Top right: pB/tB ratio at 529.5 nm from the PSI-MHD model. Bottom left: Inferred tB by correcting the K-Cor pB data (see Fig 1) with the model pB/tB ratio and limb-darkening effects (see Section 3.1). Bottom Right: Comparison between the K-Cor data and model pB.

model are shown in Figure 2, with the same polar coordinate transformation as applied to the eclipse data in Figure 1 (see Section 2.1). A direct comparison between the predicted pB and the pB observed by MLSO COSMO K-Cor (see Section 2.2) is shown in the lower right panel of the figure. The predicted and observed pB show roughly the same slope in brightness, but with the MLSO data being about 29.4% brighter on average than the model—which is just barely statistically significant given the scatter being 26.6% around the mean.

The high-resolution MHD model from PSI is useful for comparison with photometric observations of the corona (see Sections 4 and 5), which perhaps can provide insight on the limitations and constraints of the model. The model can also be used as a reasonable estimate of the polarization fraction for the K-corona scattered light. While there may be inaccuracies in the model or its assumptions (which we want to test ultimately), the polarization fraction is somewhat insensitive to the absolute values of density in the model, and is much more influenced by the geometry of the Sun and corona as extended 3D sources. We can thus use the predicted pB/tB from the PSI model combined with the observed pB from

MLSO's K-Cor to infer the expected tB of the K-corona based on the observations. This correction will create a K-Cor driven inference of tB that is directly comparable to the eclipse inference. The pB/tB ratio from the PSI model as well as the corrected tB inference based on the K-Cor data (after accounting for limb-darkening effects, see Section 3.1) are shown in the top right and bottom left panels of Figure 2 respectively.

3. K- and F-corona Inversion

The continuum data from the solar eclipse (see Section 2.1) contain emission from the K- and F-corona combined at very specific wavelengths. Hence, the relative emission observed at each bandpass will depend on the spectrum of these two continuum sources. In the inversion method presented here, we used the color spectrum (relative to the photosphere) of the F-corona to isolate the K- and F-corona contributions to the total continuum emission. The K-corona itself also has a slight color, due to the wavelength dependence of limb-darkening, and so our inversion method accounts for the color of both the

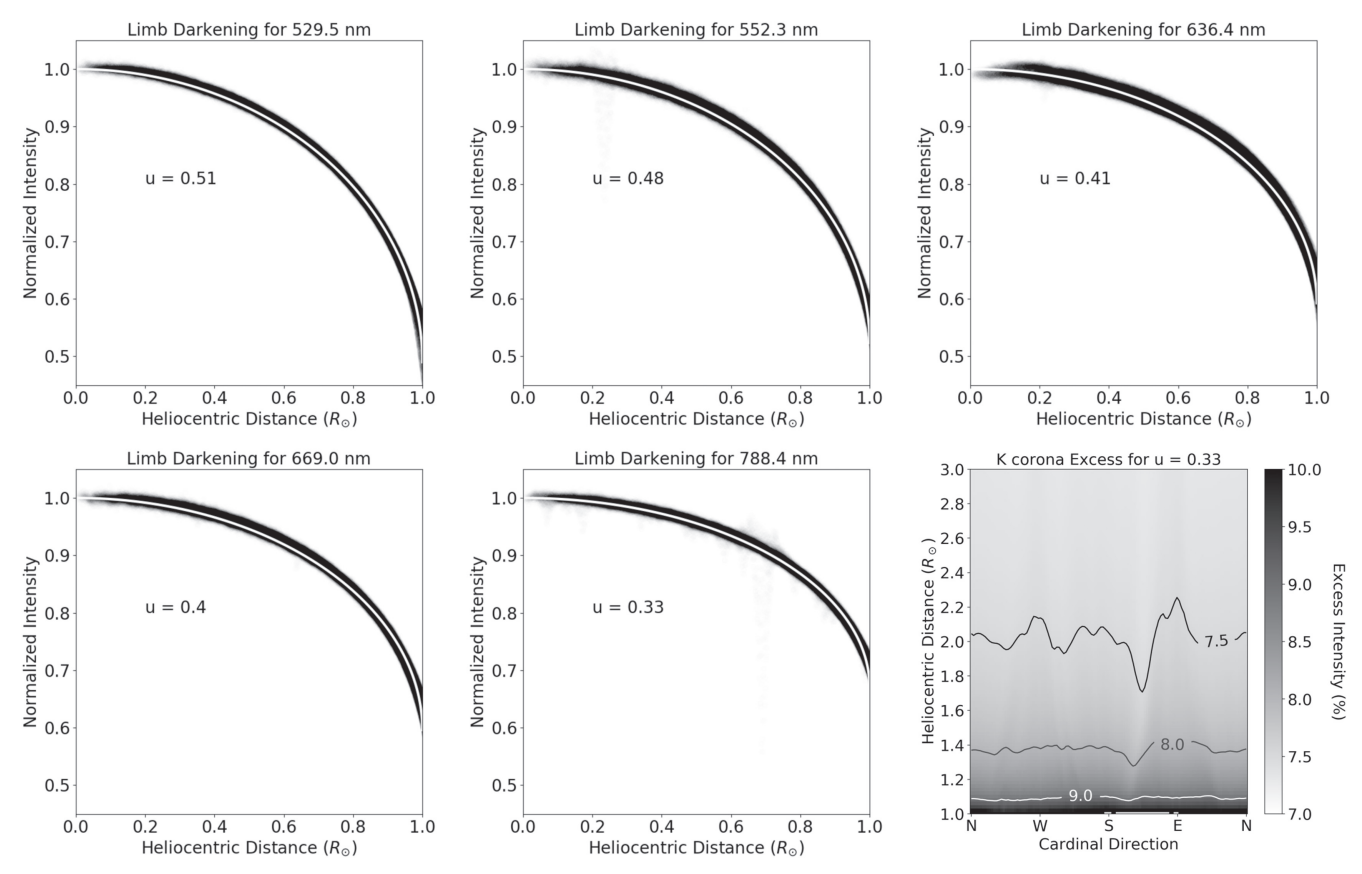


Figure 3. Limb-darkening data for each of the eclipse bandpasses, arranged in increasing wavelength. Each panel shows the observed disk intensity with black data points (normalized) as a function of the projected heliocentric distance. The overlaid white line is the best fit to the data using Equation (1), with the best-fit limbdarkening coefficient (u) noted in each panel. The bottom right panel shows the percentage of excess emission expected for 788.4 nm compared with 529.5 nm from the PSI-MHD model, after normalizing for the solar disk center intensity at each wavelength.

K- and F-corona. The determination of the K-corona color is done in Section 3.1, which is followed by the derivation of the analytical inversion approach in Section 3.2. This method is then iterated (in Section 3.3) to find the best-fit solution of the F-corona color and relative intensity of the K- and F-corona.

3.1. Limb-darkening

The surface intensity of the solar photosphere is not uniform in intensity at a given wavelength, but rather depends on the physical depth at which the solar disk is optically thick (which varies across the disk)—combined with the temperature distribution of the solar atmosphere. The photospheric radiation at the limb of the Sun is substantially fainter and redder (for visible wavelengths) than the center of the solar disk, and so this limb-darkening effect will impact the relative irradiance entering the corona in an angle-dependent manner. Thompson scattering itself has no wavelength dependence, but the angle and wavelength dependence of limb-darkening coupled with an extended 3D corona will result in a variable intensity of the K-corona at different wavelengths and heliocentric distances (e.g., Quémerais & Lamy 2002). The traditional prescription for limb-darkening (see Minnaert 1930; Howard & Tappin 2009) is given by the following:

$$I(\psi) = I_0(1 - u + u\cos\psi),\tag{1}$$

where u is the limb-darkening coefficient, and $\psi = \sin^{-1}R/R_{\odot}$ with R/R_{\odot} being the projected distance from disk center as viewed from the Earth (i.e., small-angle approximation). We refer the reader to Howard & Tappin (2009) for a full discussion on the scattering physics in the corona and the impact of limb-darkening.

To quantify the limb-darkening coefficient for each of the eclipse observations, we fit Equation (1) to observations of the solar disk performed with each of the narrowband telescopes. These solar disk observations are normally used for relative calibrations between the on- and off-band telescopes for the purposes of measuring line emission (see Section 2.1), which we are not considering here. In Figure 3, we show the observed intensity of the solar disk for each wavelength across the limb, and find the best-fit u for each. We find that the limb-darkening coefficient is decreasing with increasing wavelength, resulting in a redder limb compared with disk center (as expected). In fact, we find that the u coefficients had a simple negative linear dependence with wavelength, given by:

$$u(\lambda) = -6.8 \times 10^{-4} \left(\frac{\lambda}{\text{nm}}\right) + 0.86,$$
 (2)

with a rms error of $\sigma_{\rm rms}$ < 2.5% on the fit. Forward modeling tB from the PSI-MHD model requires a limb-darkening assumption (i.e., u), so we computed the LOS integrated K-corona intensity with the best-fit u of each bandpass. We then determined the excess emission that is expected at each bandpass relative to the lowest wavelength channel (529.5 nm), after normalizing for the solar disk center intensity at each wavelength. The color changes between the various channels are rather small, with the larger changes

occurring for larger wavelength separations. The bottom right panel in Figure 3 shows the change in intensity from the lowest to highest wavelength used in this study, which increases up to a maximum of 10% in intensity for the very low corona.

In the inversion method described in Section 3.2, we will use the PSI-MHD model prediction for the K-corona color of both pB and tB, using the best-fit coefficients from solar disk data in Figure 3. All figures in this work that show PSI-MHD model data are given for the limb-darkening coefficient at 529.5 nm. Similarly, the MLSO K-Cor pB data (see Figure 1 and Section 2.2) are presented here after a correction to pB at 529.5 nm. The correction is performed assuming u = 0.36 for 735 nm (i.e., middle of K-Cor bandpass) using the linear fit from Equation (2). The K-Cor data are then converted to tB (as shown in Figure 2) using the pB/tB ratio at 529.5 nm. The eclipse data are somewhat more complicated to correct for, as they are convolved with the F-corona intensity (which is wavelength dependent). A more careful approach is required to account for the K-corona color effect in the eclipse data, which is incorporated into the method described in Sections 3.2 and 3.3.

3.2. Method Derivation

In this section, we derive an analytical inversion method for isolating the K- and F-corona emission components for a set of total brightness observations at distinct wavelengths. First, we used the K-corona tB provided by the MLSO K-Cor data (see Section 2.2) with the pB/tB (see Section 2.3) and limb-darkening corrections (see Section 3.1) as an initial estimate of the K-corona intensity, $K = I_K(r, \theta)$, with heliocentric distance r and position angle θ of an arbitrary LOS at a reference wavelength, and in units of the solar disk center intensity. The initial cross-calibration procedure for the data was described in Section 2.1, which will be iterated later in Section 3.3.

The intensity of an arbitrary narrowband continuum eclipse image (see Section 2.1) can then be given by:

$$I_i(r,\theta) = Kd_i + Fc_i \tag{3}$$

where c_i and d_i are the color coefficients of the F- and K-corona respectively at the given wavelength, i, and $F = I_F(r, \theta)$ at the reference wavelength, similar to K above. The K-corona color term is determined by the limb-darkening analysis done in Section 3.1, and is a function of the LOS, thus $d_i = d_i(r, \theta)$. For the sake of this work, we performed the color analysis of the F-corona with respect to the 529.5 nm channel, with an intensity $I_{529.5}$ that will be used as the arbitrary reference wavelength, so $I_{529.5} = I_0$. The color of the F- and K-corona at the reference wavelength is then $c_0 \equiv 1$ and $d_0 \equiv 1$. Further, this derivation uses the assumption that all photometric observations are in units of solar disk center intensity for each arbitrary wavelength, and can be thought of simply as the scattering efficiency of each particle species for each LOS.

Solving for the F-corona at the reference wavelength is trivial if one has an estimate of the K-corona, where:

$$F = I_0 - K. \tag{4}$$

Using Equations (3) and (4) for the 529.5 nm and another arbitrary eclipse observation produces the following:

$$I_i = K d_i + (I_0 - K)c_i,$$
 (5)

then solving for the color term yields,

$$c_i = \frac{I_i - K \ d_i}{I_0 - K}.\tag{6}$$

Equation (6) thus gives a method for inferring the relative color of the F-corona by comparing an estimate of the K-corona intensity with two arbitrary narrowband observations. Because this derivation applies to a LOS in each image, the method is repeated separately for each LOS and averaged in each combination of data. That is to say, the procedure is repeated for every eclipse image relative to 529.5 nm to solve for the F-corona color, which is averaged across the entire field of view. It is possible that there could be some real color variation in the F-corona for different LOS positions, which would imply a variable dust-free zone depending on the grain species (see Section 4.1), but we will assume here that the color term is constant within our field of view ($<3~R_{\odot}$) for each wavelength. The variation in the inferred color term over the data set then enables a determination of the uncertainty of the average.

Once the color terms have been measured for the other eclipse wavelengths (i.e., Equation (6)), the relative F-corona intensity can be inferred separately using each available bandpass. The ratio between the arbitrary and reference images gives,

$$\frac{I_i}{I_0} = \frac{Kd_i + Fc_i}{K + F},\tag{7}$$

which can be rewritten to isolate the relative F-corona intensity term (i.e., $\frac{F}{K+F}$),

$$\frac{I_i}{I_0} = \left(1 - \frac{F}{K+F}\right)d_i + \frac{Fc_i}{K+F} \tag{8}$$

$$\frac{I_i}{I_0} = d_i + (c_i - d_i) \frac{F}{K + F} \tag{9}$$

and finally solved for the F-corona intensity alone, after using $I_0 = K + F$,

$$\frac{F}{K+F} = \left(\frac{I_i}{I_0} - d_i\right) \frac{1}{c_i - d_i} \tag{10}$$

$$F = (I_i - I_0 d_i) \frac{1}{c_i - d_i}$$
 (11)

Equations (4) and (11) offer two different methods to derive the same quantity, namely the relative F-corona intensity at the 529.5 nm channel. This can be done directly with the 529.5 nm channel and the K-Cor data in Equation (4), and again for every other eclipse bandpass using Equation (11).

We can then extend this procedure to isolate a new map of the K-corona (at 529.5 nm) separately, starting with a modified version of Equations (3) and (11):

$$K = \frac{I_i - Fc_i}{d_i} \tag{12}$$

$$K = \frac{I_i}{d_i} - \left(\frac{I_i}{d_i} - I_0\right) \frac{c_i}{c_i - d_i}.$$
 (13)

The technique derived in this section provides the means to isolate the relative F- and K-corona contributions as well as the relative color of the F-corona. So far, we have made the assumption that the F-corona is negligible at the base of the streamer (in the calibration wedge discussed in Section 2.1). To

address the possible F-corona offset in this calibration wedge, and the impact it has on our inversion procedure, we use an iterative method that is described in Section 3.3.

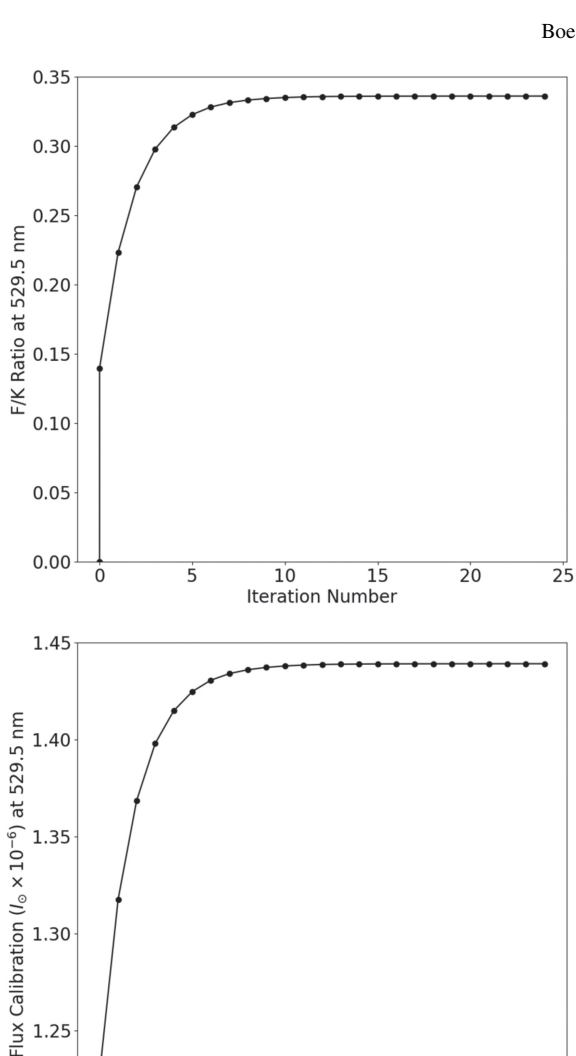
3.3. Iteration Procedure

The process described in the previous section works for coronal regions where the data are reliable between all data sets. For the eclipse data, we can observe emission typically between about 1.05 up to 3 R_{\odot} . The K-Cor data are not as extended, however, as they must contend with the high sky brightness that is present in the absence of a TSE. Additionally, this procedure initially assumes that there is no F-corona contribution to the calibration wedge (see Section 2.1) in the low region of the eastern streamer, because the F-corona offset is initially difficult to immediately estimate without an additional constraint.

We thus use an iterative process that will isolate the K- and F-corona intensity. The first iteration uses the MLSO K-Cor data as the initial K-corona intensity, $I_K(r, \theta)$, and solves for K and F using the 529.5 nm eclipse data and an arbitrary bandpass. Each other eclipse bandpass repeats this procedure separately, as I_i , which then yields a different color term for each channel, c_i . Each of the other bandpasses is then used to independently generate an inferred map of K and F at 529.5 nm. After each iteration, we have an estimated color for each bandpass and an average map of the K- and F-corona. The newly inferred map of the K-corona is then used as the input for $I_{\kappa}(r, \theta)$ in the next iterative step. In this way, we can use the MLSO K-Cor data as a calibration source and as a means to create an initial estimate of the color terms and K-corona intensity.

Next, we take the inferred F-corona map (from Equation (11)) and fold it twice along the polar and equatorial axes. The result is a latitude averaged, axis-symmetric map of the F-corona. The relative F/K intensity is then measured inside the original calibration wedge, and is used to estimate the F-corona contribution to the brightness inside this calibration wedge (i.e., the flux calibration, see Section 2.1), which in the first iteration had been assumed not to have any F-corona intensity. The inferred excess intensity is added to the original data to recalibrate the images based on the new best guess of the colors and F/K offset in the calibration box. In addition to correcting the F/K offset at each iteration, we correct for the limb-darkening effect on the calibration—that is, we account for the excess intensity expected in the K-corona at the different wavelength channels given the F/K ratio and K-corona emission in the calibration box. The newly calibrated data combined with the inferred K-corona map are used to repeat the entire procedure of Section 3.2. After several iterations, the F-corona offset and inferred colors settle on the most probable solution, because the F- and K-corona remain constant under the assumption that the F-corona is axis-symmetric around both the poles and equator. Values for the F/K offset in the calibration wedge, the flux calibration correction, and inferred colors for each iterative step are shown in Figure 4.

We performed a total of 25 iterations, at which point the solution did not vary within the photometric uncertainty. The value of the F/K ratio changed a lot initially, but quickly converged to a value of 0.336 ± 0.006 (the uncertainty is determined by measuring the scatter of the inference for the pixels inside the calibration wedge). Despite the changing F/K offset, the colors at each iteration are rather stable. The scatter (and thus the inferred uncertainty) of the color values drops after a couple of iterations while remaining within about 2σ of the original estimate (from the K-Cor data). The colors do



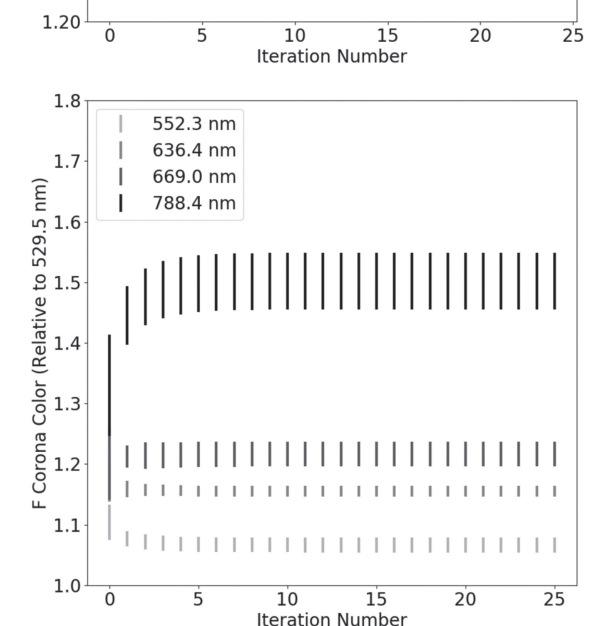


Figure 4. Top: F/K ratio for 529.5 nm inferred in the calibration wedge (see Section 2.1) over 25 iterations (see Section 3). Middle: Flux calibration for 529.5 nm in the calibration wedge after each iteration; other wavelengths have their calibration account for the K- and F-corona colors (see Sections 3.1 and 3.3). Bottom: Corresponding estimate of the F-corona colors for each observed wavelength over the iterations.

1.25

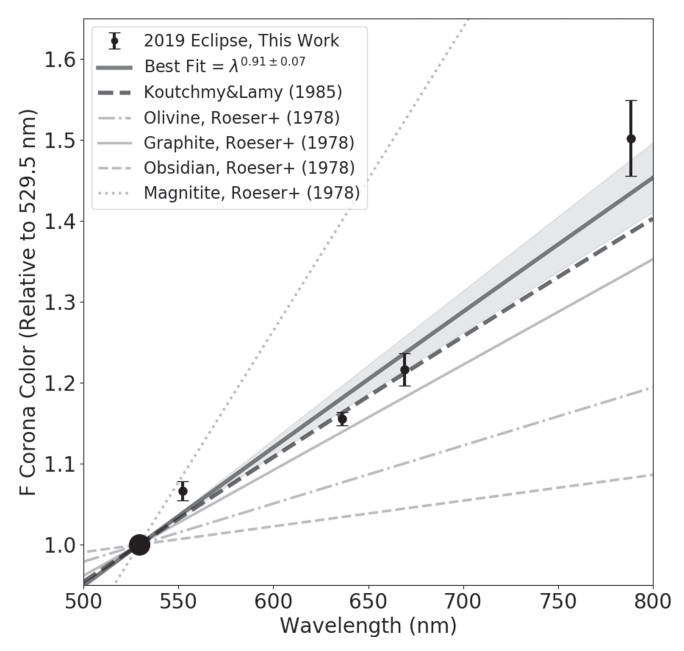


Figure 5. Final inference of the F-corona color spectrum using the method outlined in Section 3. The solid line and the shaded region show the best-fit power law and uncertainty of the spectrum based on our analysis. The bold dashed line shows the spectrum presented in Koutchmy & Lamy (1985), while the set of thin gray lines shows the predicted spectrum for the F-corona given different dust compositions from Roeser & Staude (1978).

spread out slightly from the initial estimate, with the lowest wavelength channel slightly decreasing in the inferred color, and vice versa for the highest wavelength.

4. Results

The novel K- and F-corona inversion technique introduced here (in Section 3) provides an inference of the F-corona color spectrum (Section 4.1) as well as the spatially resolved total brightness of both the K (Section 4.2) and F (Section 4.3) components of the coronal continuum emission. What follows is a discussion of the results from this inversion technique applied to the 2019 July 2 TSE data (see Section 2.1), as well as the simultaneous MLSO COSMO K-Cor observations (see Section 2.2). These results are then compared with the PSI-MHD model prediction of the eclipse corona (see Section 2.3) and various historical works. In general, all data sets and the model are reasonably consistent with one another and with previous studies, but there are some interesting deviations that could have implications for the nature of the F-corona.

4.1. F-corona Color

The final inferred color spectrum of the F-corona from our inversion method is shown in Figure 5. A power-law fit to the data gives $I_F \propto \lambda^{0.91\pm0.07}$, which is roughly consistent with a linear dependence of the color spectrum for visible wavelengths. The fit to our inferred F-corona spectrum is broadly consistent with the slope given by Koutchmy & Lamy (1985), which is itself a fit to a few earlier observational studies. Both fits are somewhat close to the predicted spectrum if the F-corona is dominated by graphite grains (Roeser & Staude 1978). Graphite grains are expected to be the dominant grain at about 4 R_{\odot} (Mukai et al. 1974) given the dust evaporation (i.e., dust-free zone), which is expected to be variable depending on the grain composition (and thus should be elongation dependent).

The reddest data point, 788.4 nm, is noticeably higher than the best-fit power law, perhaps indicating that the slope of the F-corona color spectrum may steepen in the infrared. Such a steepening is expected at longer wavelengths (>1 μ m) due to thermal emission of the dust (e.g., Kimura & Mann 1998). The precise nature of the F-corona color at different elongations is not well known, though previous work has indicated a shallower slope in the zodiacal light at high elongations compared with the F-corona (see Koutchmy & Lamy 1985 and therein). It is difficult to make definitive statements on the nature of the F-corona from the existing observations, as most studies have probed only an inner elongation of about 4 R_{\odot} . Thus, the nature of the inner F-corona is still largely unknown. Perhaps the color spectrum starts with a steeper slope in the inner corona and becomes shallower at higher elongations, which could be caused by thermal emission of particularly hot dust near the Sun at the edge of the dust-free zone. It is entirely possible that a mix of spatially variable grain species distributions and some component of thermal emission near 1 μ m may contribute to the precise color slope of the F-corona in the near-infrared. Future work should endeavor to resolve the color spectrum of the F-corona across a wide range of wavelengths, and look for spatially dependent changes that would indicate variability in the thermal emission, mineralogy, and/or size distribution of dust in the F-corona and zodiacal light.

An important consequence of the value of the color slope in this study, and in previous work, is that one must be careful when considering F-corona emission over different wavelengths. A polarization inversion method at 800 nm will certainly arrive at a different F-corona intensity than an identical one performed at 500 nm, by a factor of about 50%. Such a color dynamic could also affect the inferred polarization ratio of the K-corona, as there will be a different background unpolarized brightness (due to the F-corona) at different wavelengths across the visible spectrum. One must account for both the color of the F-corona and K-corona (from limb-darkening, see Section 3.1) to correctly quantify K- and F-corona emission.

It is worth noting that the tB inferred by our color-based inversion method is rather insensitive to the precise result of the F-corona color slope and F-corona calibration offset (see Section 3), because it is taken simply as the colorless component of emission between our observables across the visible spectrum (after accounting for limb-darkening effects, see Section 3.1). This colorless component remains almost exactly the same regardless of assumptions about the F-corona, which is a strength for this method of inversion. Any uncertainty in the calibration offset simply shifts the relative brightness of the F-corona (as addressed in Section 3.3), which acts to shift the entire image up or down by a constant value. Thus, the colorless component of the emission remains unchanged in the inference, while the colored component can be stretched based on the offset. Our final results are thus robust in inferring the K-corona tB signal, while the inferred F/K offset needs only to assume axis-symmetric F-corona emission to converge quickly on the best-fit offset.

4.2. K-corona Total and Polarized Brightness

The K-corona total brightness (*tB*) inferred from the 2019 July 2 TSE (see Section 2.1) is shown in a collection of radial scans in the left panels of Figure 6, along with some comparisons to the literature and the PSI-MHD model (see Section 2.3). The spatially

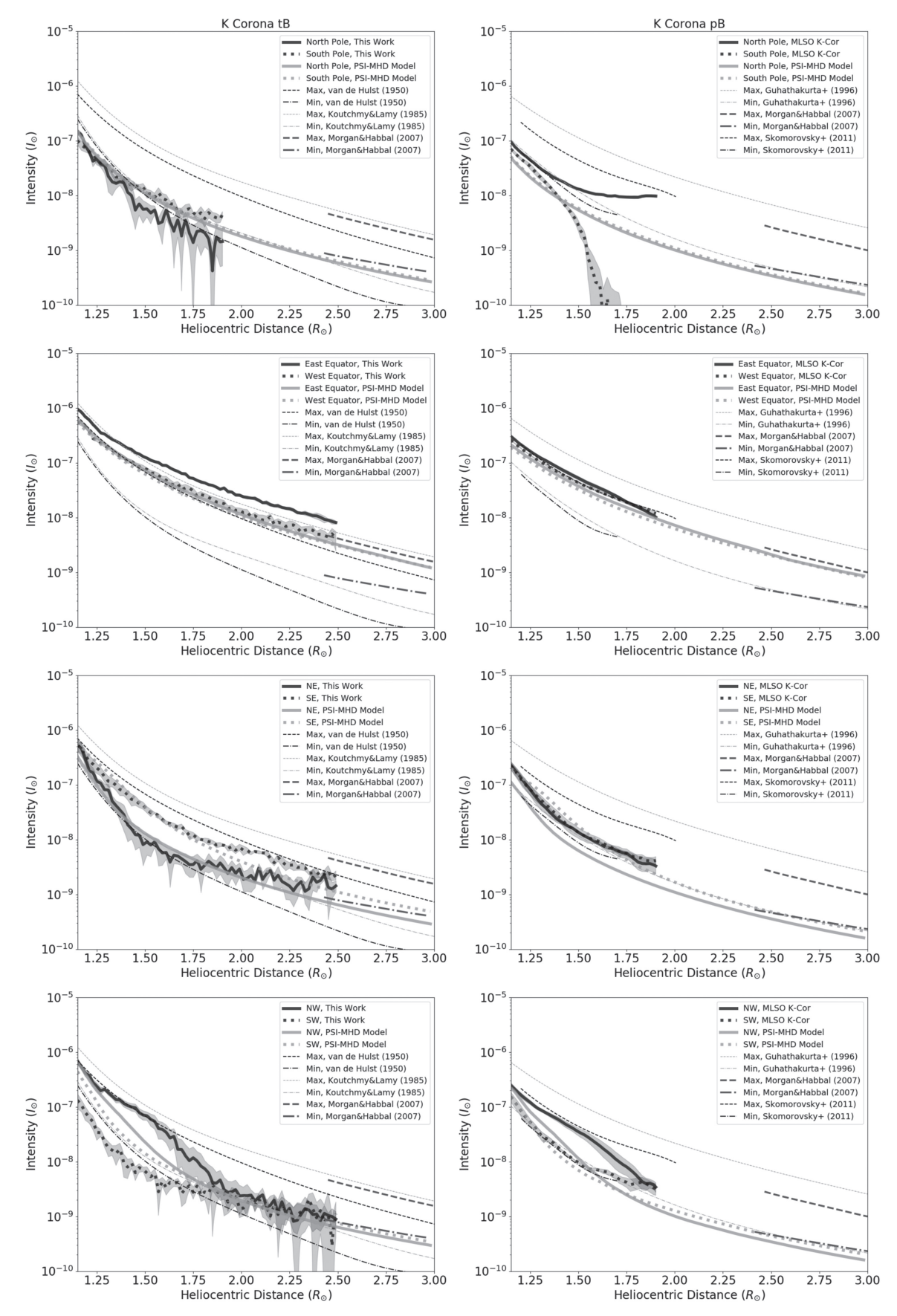


Figure 6. Left panels show radial scans of the K-corona *tB* from the inversion technique (see Section 3), for a collection of different latitude regions. All scans are done inside 15° wedges centered on the cardinal direction noted in the legends of each panel. The right panels show the same scans for the K-corona *pB* from MLSO's K-Cor (see Section 2.2). A collection of literature values and the PSI-MHD model prediction (see Section 2.3) for this eclipse is also shown for comparison.

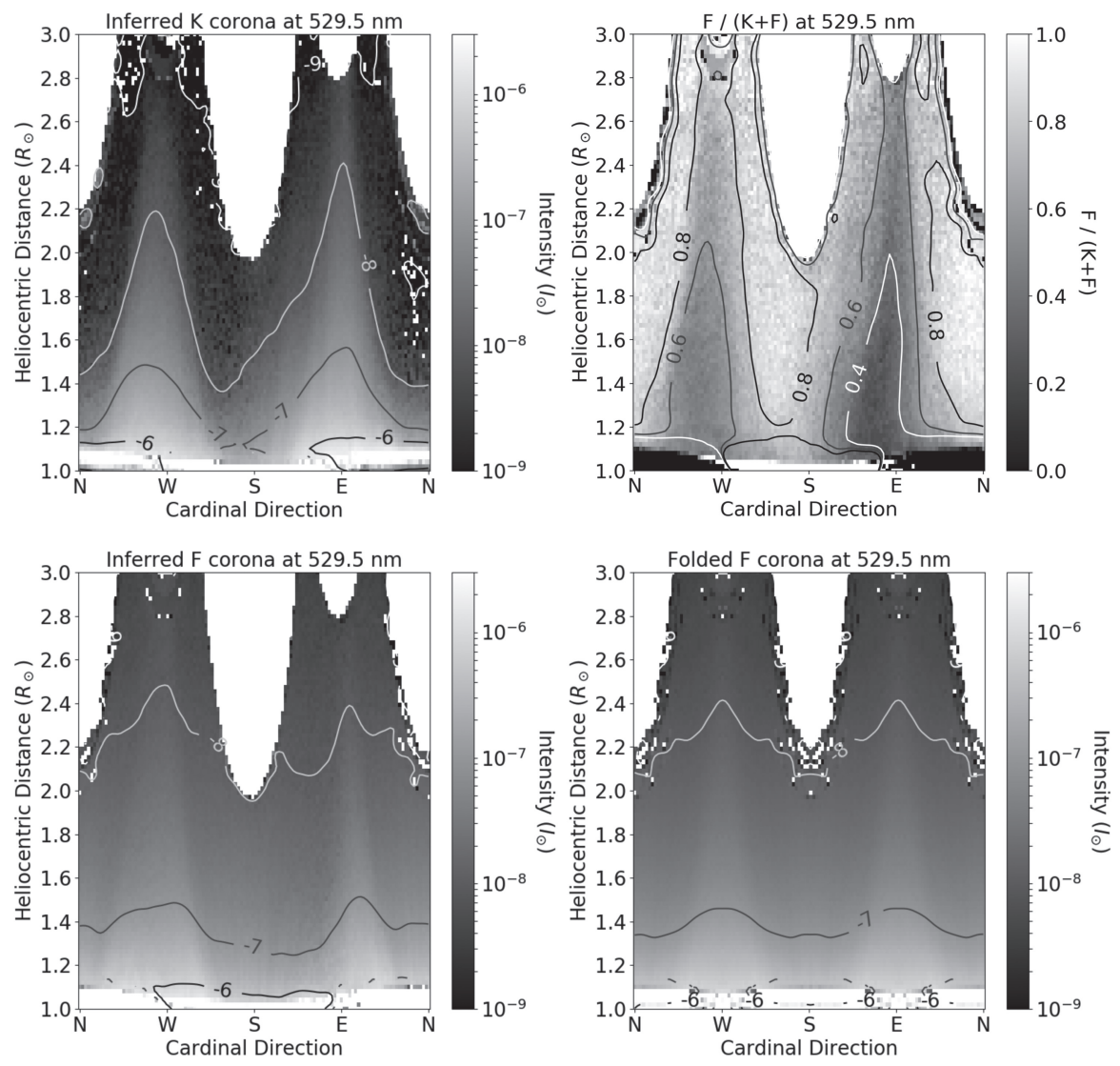


Figure 7. Top left: Final inferred K-corona tB, from the procedure described in Section 3. Top right: Inferred F/(K+F) ratio at 529.5 nm. Bottom left: Final inferred F-corona brightness at 529.5 nm. Bottom right: Axis-symmetric average of the F-corona inference.

resolved K-corona inference is given in the top left panel of Figure 7. Traces of the K-corona intensity at a set of fixed radial distances are shown in Figure 8, in addition to direct LOS intensity comparisons between the eclipse, the MLSO K-Cor observations, and the PSI predictions.

In general, we find a K-corona tB that is consistent with the range of values typically found in the corona. For example, the streamers have a substantially higher ($\sim 10 \times \text{at} \ 1.5 \ R_{\odot}$) intensity than the poles, as expected, and the highest and lowest intensities broadly agree with the higher and lower estimates from the literature (i.e., van de Hulst 1950; Koutchmy & Lamy 1985; Morgan & Habbal 2007). Similarly, the MLSO K-Cor observations (see Section 2.2) on the day of the eclipse are consistent with previous work on the polarized brightness (pB) of the K-corona (i.e., Guhathakurta et al. 1996; Morgan & Habbal 2007; Skomorovsky et al. 2011), which are shown in the right panels of Figure 6. The comparison to Skomorovsky et al. (2011) is especially interesting, as they observed the K-corona pB during the 2008 TSE, close to solar minimum (much like this 2019 eclipse). Further, the MLSO K-Cor data appear to be rather robust in the equatorial

streamers out to about $1.8~R_{\odot}$, but they diverge rather quickly in the lower-intensity regions near the poles of the Sun (top right panel of Figure 6), and perhaps are only accurate to a distance of about $1.2-1.3~R_{\odot}$. Regardless, the MLSO data set is a valuable and essential component to this work (as the calibration source and initial guess of the K-corona), and can be used for detailed analysis of the lower regions of the corona.

Of course, there are a multitude of studies that have observed the K-corona *pB* and *tB* intensity, either through direct observation of the F-corona lines (e.g., van de Hulst 1950) or via polarization observations. The polarization observations, in particular, have been repeated many times with both eclipses (e.g., Guhathakurta et al. 1996; Skomorovsky et al. 2011) and coronagraphic data sets (e.g., Morgan & Habbal 2007; Lamy et al. 2020). To compare our K-corona intensity results with other studies, we have chosen a small number for the sake of brevity and clarity, especially given that the decades of work have consistently reproduced the same intensities within a range that is comparable to the real physical variation of the electron density over the solar cycle and across different coronal structures (e.g., streamers versus coronal holes).

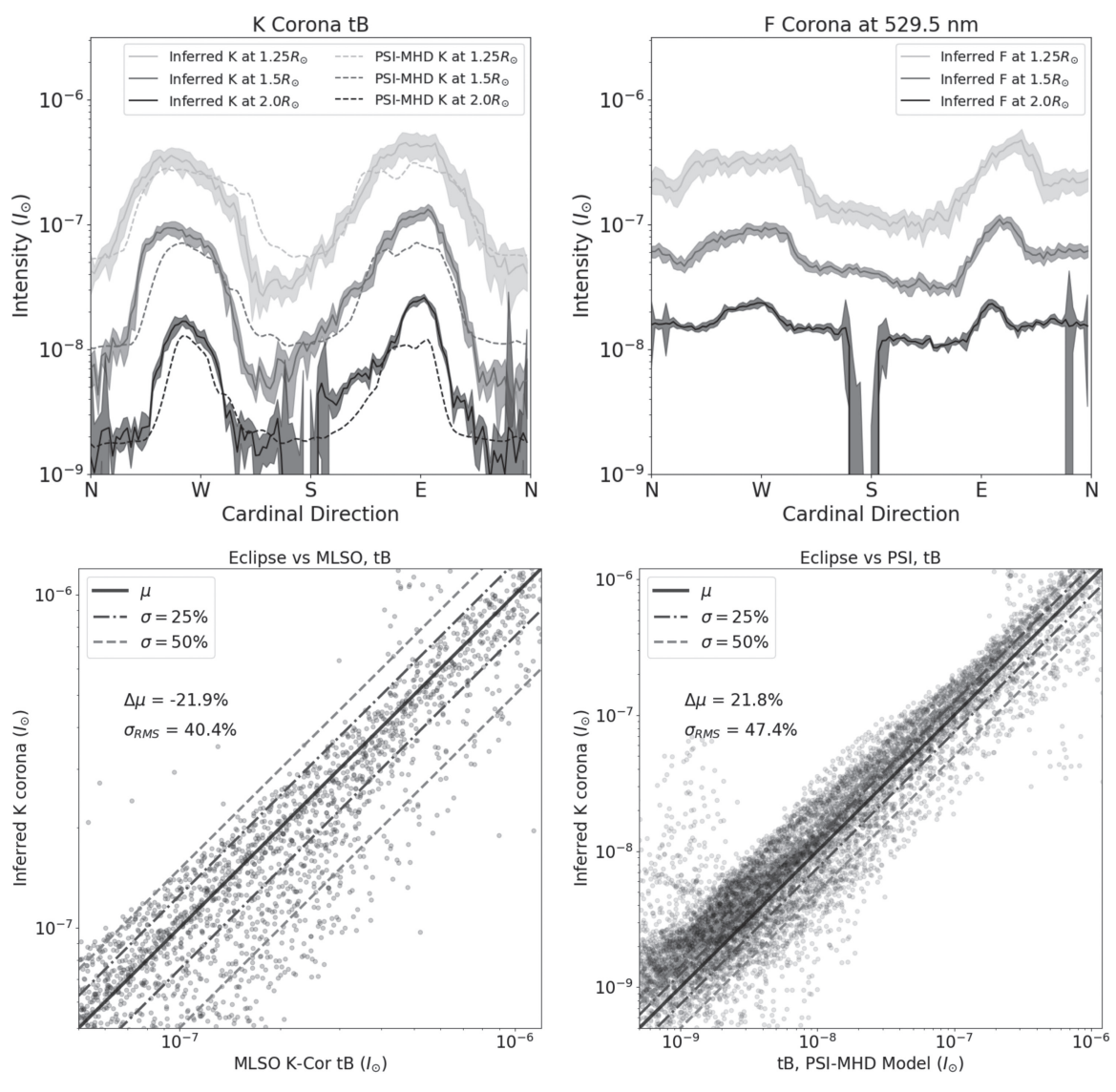


Figure 8. Top left: Traces at 1.25, 1.5, and 2.0 R_{\odot} (scan width of 0.1 R_{\odot}) of the inferred K-corona tB along with the PSI-MHD model prediction of tB (see Section 2.3). Top right: Same as the top left, but for the inferred F-corona emission at 529.5 nm. Bottom left: Direct comparison between the inferred K-corona tB and the K-Cor corrected tB (from pB and pB/tB, see Section 2.2). Bottom right: Direct comparison between the inferred K-corona tB and the PSI-MHD model prediction of tB.

In addition to finding a K-corona intensity that is consistent with previously published values, we find that the PSI model for this specific eclipse matches the data reasonably well. A direct comparison for each LOS between our inferred K-corona tB and both the pB/tB corrected K-Cor data (as in Figure 2) and the PSI-MHD model prediction are shown in the bottom panels of Figure 8. We find a very close match between the PSI model and our inferred K-corona tB, with only an 21.8% average disagreement down to a brightness of $10^{-8}I_{\odot}$. The scatter between the data sets is substantially higher, at about 47.4%. This scatter is expected even if the physics of the model were perfect, because the coronal morphology of the model is largely determined by the surface boundary conditions, which are comprised of observations made in the weeks prior to the eclipse (as mentioned in Section 2.3). In this sense, the surface magnetic field of the model cannot perfectly match the instantaneous surface flux distribution during the eclipse, because some discrepancies between streamer shapes and locations are expected. The polar magnetic flux, which has strong effects on the precise

angle of streamers in the final prediction (Riley et al. 2019), is also not well constrained. This collection of effects is more than sufficient to explain the scatter between the model and our data.

There is an interesting anomaly between our inferred K-corona tB and the PSI model prediction in the northwest scan (bottom left panel of Figure 6), where our inferred K-corona remains at a higher intensity until a distance of about $1.8\ R_{\odot}$. This "bump" in intensity might seem as though there could be some issue with the observational data, but we see a bump in the same location in the K-Cor pB observation (bottom right panel of Figure 6). Seeing this feature in both of the entirely independent observations hints that this is some real feature in the corona that is not seen in the model, indicating a morphology or boundary condition mismatch.

Once the K-Cor data are corrected with the pB/tB fraction from the PSI model (see Section 2.3), they match the eclipse data very well. There is an average difference of 21.9% between the eclipse and K-Cor data sets, with the inferred eclipse intensity being fainter than K-cor. This difference could be explained by an

additional pB signal that is contaminating the K-Cor data, such as some unaccounted pB signal from the Earth's atmosphere, or could perhaps indicate a slight pB signal from the F-corona for low elongations (see Section 4.3). It is also worth considering that the overall scatter in the cross-match is 40.4%, which could imply that photometric uncertainties and/or issues in the model pB/tB correction may be sufficient to explain the difference between these data sets. In the next section, we expand on this possibility that the F-corona itself may have a slight pB component in the lower regions of the corona that is causing this pB excess, as part of a broader F-corona intensity discussion.

4.3. F-corona Brightness

Our inference of the F-corona intensity at 529.5 nm is shown in Figure 7. The bottom left panel of the figure shows the spatially resolved F-corona map, while the bottom right panel shows the same data, except with folding across the polar and equator axis. The folded F-corona looks rather similar to the unfolded one, so the folded version is likely a good estimate of what the F-corona really looks like. This similarity supports the initial assumption for using the folded F-corona as a method for inferring the F-corona offset in the calibration procedure (see Section 3.3). We find that the F-corona is slightly higher near the equator than at the poles, as demonstrated by the F-corona intensity traces shown in the top right panel of Figure 8. This difference between the polar and equatorial F-corona has been noted before (e.g., Koutchmy & Lamy 1985; Morgan & Habbal 2007; Lamy et al. 2020), though older work including van de Hulst (1950) and others of that period assumed that the F-corona was uniform for all solar latitudes, which is increasingly clear to be incorrect.

There are some slight anisotropies between the northern and southern polar regions, where the northern latitudes seem to have a higher F-corona intensity and a lower K-corona intensity (shown in Figure 7, see Section 4.2). It is perhaps possible that there could be some variation in the inner regions of the F-corona due to a physical interaction between the K- and F-corona (i.e., collisions, B field, etc.). It could also be interpreted as implications on the dust-size or grain-composition distributions or variation in the dust-free zone. However, it is more likely that this is an effect from slight errors in the synthesis procedure of this work, as the variance between similar latitudinal regions is rather small compared with the overall differences between the F- and K-corona profiles at different distances. More data of this type are required across a solar cycle to investigate if there are small changes in the F-corona that correlate with K-corona emission.

The relative F-corona intensity of the total continuum signal is shown in the top right panel of Figure 7. These F/(K+F) values are quite high, at about 0.3–0.5 at the lowest in the eastern streamer, then rising to about 0.8 at a distance as low as 1.25 R_{\odot} in the polar coronal holes. This large contribution of the F-corona partly explains why the polarization observations of K-Cor (see Sections 2.2 and 4.2) are not able to probe farther than about 1.3 R_{\odot} in the polar regions, as the vast majority of the photometric signal is originating from the unpolarized (or perhaps slightly polarized) F-corona. The high F-corona fraction is no doubt a result of the Sun being almost precisely at solar minimum during the 2019 July 2 TSE. We expect the electron density to be at its lowest overall in the corona during this time, while the F-corona has been observed to be rather invariant over the solar cycle (Morgan & Habbal 2007). The

high F-corona fraction during this solar minimum corona also increases the confidence in our ability to quantify the color of the F-corona between the channels (as presented in Section 4.1), as it is a large fraction of the overall intensity. The results of this work could thus be generalized to other periods of the solar cycle to remove the F-corona signal and enable a more complete study of the total K-corona intensity.

The overall intensity of the F-corona agrees reasonably well with previous published work, as can be seen in the radial scans shown in Figure 9. We do find that the F-corona is considerably brighter than Koutchmy & Lamy (1985), but is rather similar to van de Hulst (1950) in the coronal poles. Our results match rather well with Morgan & Habbal (2007), who inferred the F-corona via pB and tB observations of LASCO-C2 (thus at high elongations, $>2.4 R_{\odot}$). The historical work of van de Hulst (1950) used Fraunhofer line depths (see Section 1) in contrast to the polarization method of Koutchmy & Lamy (1985) and Morgan & Habbal (2007). At high elongations, it has been observed that the F-corona is essentially unpolarized (e.g., see Koutchmy & Lamy 1985; Lamy et al. 2020 and therein), but it is somewhat uncertain in the low corona. However, recent work by Morgan & Cook (2020) did infer a slight polarization fraction in the F-corona of around 5%-8% at a heliocentric distance of 4-5.5 R_{\odot} , using LASCO-C2 observations.

If the F-corona does have a substantial polarization fraction in its emission at low elongations, there could be a bias in the pB inferred F-corona intensity and thus would explain why our color-tB inversion method is finding a higher F-corona intensity, but would not affect the F-line depth analysis of van de Hulst (1950). The lower regions of the corona also have the lowest polarization fraction from the K-corona (see Figure 2), so any contribution from a small polarized dust signal in the F-corona at low elongations could contribute excess intensity to pB observations that is normally attributed entirely to the K-corona. If the F-corona is indeed dominated by diffracted light from large particles (compared with visible wavelengths), then Lamy et al. (2020) claims it is safe to assume essentially no polarized component of F-corona emission. If there are perhaps some smaller dust grains near the Sun that are directly scattering (rather than only a diffraction contribution), then we would expect some amount of F-corona polarization near the Sun (per the argument of Koutchmy & Lamy 1985).

The excess of our inferred F-corona signal for the low corona (based on the color), combined with the excess of *pB* intensity seen in the MLSO K-Cor data compared with the eclipse data (see Section 4.2) both seem to indicate that the F-corona may be slightly polarized. The MLSO K-Cor data are also taken between 720 and 750 nm, where we have demonstrated that the F-corona is a reasonably large fraction of the total brightness; this eclipse being almost exactly at solar minimum enhances any contribution from the F-corona due to the low electron density of the corona at solar minimum.

There could also be some solar cycle variation of the F-corona in the very low corona. Some sort of physical (i.e., n_e , T_e , B, etc.) variation in the corona driven by the solar cycle could possibly shift the distance of the dust-free zone (see Sections 1, 4.1). If the dust-free zone moves inward during solar minimum, we would expect more scattered light in the corona near the Sun (even if it is still somewhat out of the plane of sky)—which would also enhance any pB effects that may be

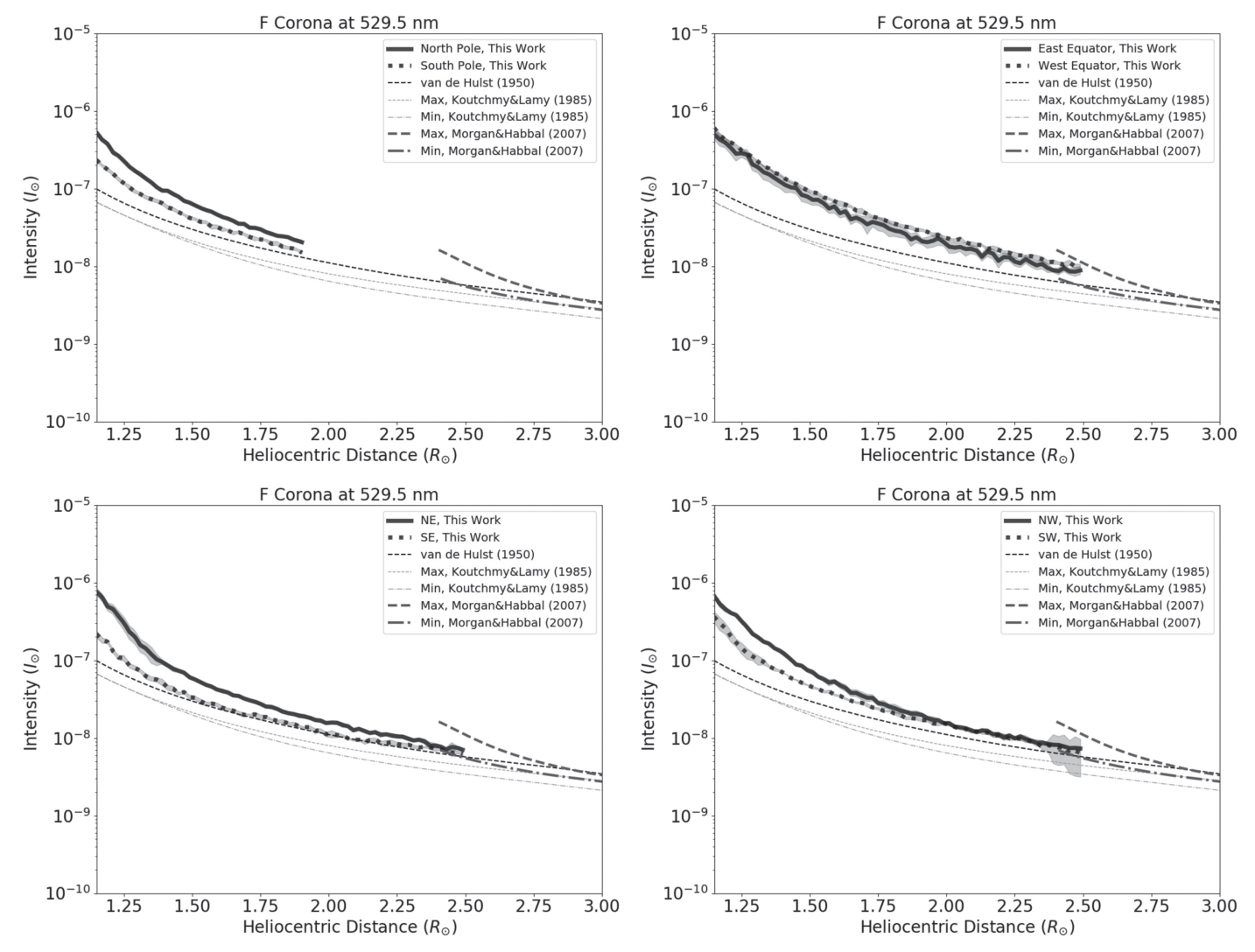


Figure 9. Radial scans of the F-corona total brightness from the inversion technique (see Section 3), for a collection of different latitude regions (same style as Figure 6). All scans are done inside 15° wedges centered on the cardinal direction noted in the legends of each panel. A collection of literature values is also shown for comparison.

present in the F-corona, as well as increase the overall F-corona intensity. Additional studies are no doubt required to test these possibilities further, especially one where both the color and *pB* brightness can be observed simultaneously at a TSE. Off-limb observations by the new Daniel K. Inouye Solar Telescope (DKIST; Tritschler et al. 2016) observatory may also help to address this problem.

5. Conclusions

We have presented a new inversion technique (Section 3) that extracts the K- and F-corona total brightness (t_B , see Sections 4.2 and 4.3) and F-corona color (see Section 4.1) using a set of narrowband TSE observations across the visible spectrum (see Section 2.1). Our results are broadly consistent with previous work, as well as the MLSO COSMO K-Cor coronagraph observations (see Section 2.2) and the state-of-the-art PSI-MHD model prediction (see Section 2.3). We find that the eclipse and K-Cor data are roughly in agreement out to $\sim 1.3~R_{\odot}$ in the coronal holes, and up to $1.8~R_{\odot}$ in the streamers, highlighting that the MLSO COSMO K-Cor data are a robust data set for studying the lower regions of the corona, in the absence of an eclipse.

The major conclusions from this work include:

- 1. The F-corona color spectrum is found to be consistent with that of Koutchmy & Lamy (1985), with a best-fit power law of $I_F \propto \lambda^{0.91 \pm 0.07}$ for visible wavelengths.
- 2. The F-corona brightness is found to be nonuniform with latitude (as noted in previous studies), where the equatorial regions have a higher F-corona intensity compared with the poles.
- 3. We find that the F-corona brightness is significantly higher in the low corona (see Figure 9) than found in previous studies, but our inference matches the literature very well beyond about $1.5\ R_{\odot}$. This finding may indicate that the nature of the dust-free zone varies with solar cycle, or perhaps that the F-corona has a polarized brightness component that is unaccounted for in pB driven inversions.
- 4. The eclipse driven K-corona inversion matches the PSI-MHD model very well out to high heliocentric distances. The close match between the model and observations indicates that the model is doing an excellent job at predicting the K-corona, and thus is likely generating a reasonable electron density for the corona in 3D.

The results presented here support the need for further photometric color analysis of the corona as a tool to study the F-corona. There are potentially unexplored avenues to constrain the dust-free zone, as well as the dust distribution and the far-versus-near component of the F-corona scattering (i.e., scattering versus diffraction, see Section 4.1). Further, this study emphasizes the importance of narrowband observations of the corona, which could be performed with future groundand space-based coronagraphs. These coronagraphs should utilize narrowband filters to probe not only ionic line emission, but also the color of the coronal continuum emission. Even with recent advancements in instrumentation. TSEs continue to provide unparalleled access to the corona continuously from just above the solar surface out to at least 2.5 R_{\odot} . At present, no existing telescope can rival the coronal view provided by a TSE.

We thank all the observers that performed the narrowband observations at the 2019 July 2 total solar eclipse (see Table 1). The K-Cor data were courtesy of the Mauna Loa Solar Observatory, operated by the High Altitude Observatory, as part of the National Center for Atmospheric Research (NCAR). NCAR is supported by the National Science Foundation.

Financial support was provided to B. Boe by the National Science Foundation under Award No. 2028173, and by AURA/NSO with grant N97991C to the Institute for Astronomy at the University of Hawaii. S.H. and the 2019 eclipse expedition were supported under NSF grant AST-1733542 to the Institute for Astronomy of the University of Hawaii. C.D. was supported by NASA grants 80NSSC18K1129 and 80NSSC20K1285. M.D. was supported by the Grant Agency of Brno University of Technology, project No. FSI-S-20-6187.

ORCID iDs

```
Benjamin Boe  https://orcid.org/0000-0002-6396-8209 Shadia Habbal  https://orcid.org/0000-0003-4089-9316 Cooper Downs  https://orcid.org/0000-0003-1759-4354
```

References

```
Agrawal, D. C. 2016, EJPh, 37, 035601
Allen, C. W. 1947, MNRAS, 107, 426
Baumbach, S. 1938, AN, 267, 273
```

```
Boe, B., Habbal, S., Druckmüller, M., et al. 2018, ApJ, 859, 155
Boe, B., Habbal, S., Druckmüller, M., et al. 2020a, ApJ, 888, 100
Boe, B., Habbal, S., & Druckmüller, M. 2020b, ApJ, 895, 123
Colaninno, R. C., & Vourlidas, A. 2009, ApJ, 698, 852
Cram, L. E. 1976, SoPh, 48, 3
DeForest, C. E., de Koning, C. A., & Elliott, H. A. 2017, ApJ, 850, 130
Del Zanna, G., Gupta, G. R., & Mason, H. E. 2019, A&A, 631, A163
Dere, K. P., Wang, D., & Howard, R. 2005, ApJL, 620, L119
Ding, A., & Habbal, S. R. 2017, ApJL, 842, L7
Druckmüller, M. 2009, ApJ, 706, 1605
Guhathakurta, M., Holzer, T. E., & MacQueen, R. M. 1996, ApJ, 458, 817
Habbal, S. R., Druckmüller, M., Morgan, H., et al. 2011, ApJ, 734, 120
Habbal, S. R., Morgan, H., Druckmüller, M., et al. 2013, SoPh, 285, 9
Hayes, A. P., Vourlidas, A., & Howard, R. A. 2001, ApJ, 548, 1081
Hou, J., de Wijn, A. G., & Tomczyk, S. 2013, ApJ, 774, 85
Howard, R. A., Vourlidas, A., Bothmer, V., et al. 2019, Natur, 576, 232
Howard, T. A., & Tappin, S. J. 2009, SSRv, 147, 31
Kimura, H., & Mann, I. 1998, EP&S, 50, 493
Koutchmy, S., & Lamy, P. L. 1985, in IAU Coll. 85: Properties and
  Interactions of Interplanetary Dust, ed. R. H. Giese & P. Lamy (Dordrecht:
  Springer), 63
Kramar, M., Airapetian, V., Mikić, Z., & Davila, J. 2014, SoPh, 289, 2927
Lamy, P., Floyd, O., Mikić, Z., & Riley, P. 2019, SoPh, 294, 162
Lamy, P., Llebaria, A., Boclet, B., et al. 2020, SoPh, 295, 89
Lamy, P. L. 1974, A&A, 33, 191
Landi, E., Del Zanna, G., Young, P. R., Dere, K. P., & Mason, H. E. 2012,
   ApJ, 744, 99
Leinert, C., & Grün, E. 1990, in Interplanetary Dust, ed. R. Schwenn &
  E. Marsch (Heidelberg: Springer), 207
Mann, I. 1998, EP&S, 50, 465
Mikić, Z., Downs, C., Linker, J. A., et al. 2018, NatAs, 2, 913
Minnaert, M. 1930, ZAp, 1, 209
Moran, T. G., & Davila, J. M. 2004, Sci, 305, 66
Moran, T. G., Davila, J. M., & Thompson, W. T. 2010, ApJ, 712, 453
Morgan, H., & Cook, A. C. 2020, ApJ, 893, 57
Morgan, H., & Habbal, S. R. 2007, A&A, 471, L47
Mukai, T., Yamamoto, T., Hasegawa, H., Fujiwara, A., & Koike, C. 1974,
  PASJ. 26, 445
Ney, E. P., Huch, W. F., Kellogg, P. J., Stein, W., & Gillett, F. 1961, ApJ,
  133, 616
Quémerais, E., & Lamy, P. 2002, A&A, 393, 295
Reginald, N. L., Cyr, O. C. S., Davila, J. M., & Brosius, J. W. 2003, ApJ,
  599, 596
Reginald, N. L., St., Cyr, O. C., Davila, J. M., et al. 2009, SoPh, 260, 347
Riley, P., Linker, J. A., Mikic, Z., et al. 2019, ApJ, 884, 18
Roeser, S., & Staude, H. J. 1978, A&A, 67, 381
Scherrer, P. H., Schou, J., Bush, R. I., et al. 2012, SoPh, 275, 207
Schmelz, J. T., Reames, D. V., von Steiger, R., & Basu, S. 2012, ApJ, 755, 33
Skomorovsky, V. I., Trifonov, V. D., Mashinch, G. P., et al. 2011, Ge&Ae,
  51, 1063
Tritschler, A., Rimmele, T. R., Berukoff, S., et al. 2016, AN, 337, 1064
van de Hulst, H. C. 1947, ApJ, 105, 471
van de Hulst, H. C. 1950, BAN, 11, 135
```